

Molecular Engineering for Large Open-Circuit Voltage and Low Energy Loss in Around 10% Non-fullerene Organic Photovoltaics

Bo He,^{†,‡,§} Bin Yang,^{*,†,‡,#} Matthew A. Kolaczowski,[†] Christopher A. Anderson,[†] Liana M. Klivansky,[†] Teresa L. Chen,[†] Michael A. Brady,^{†,§} and Yi Liu^{*,†,§}

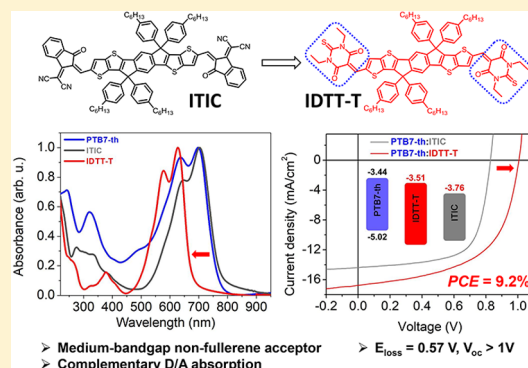
[†]The Molecular Foundry, Lawrence Berkeley National Laboratory, Berkeley, California 94720, United States

[#]College of Materials Science and Engineering, Key Laboratory for Micro-Nano Physics and Technology of Hunan Province, Hunan University, Changsha, Hunan 410082, China

[§]Advanced Light Source, Lawrence Berkeley National Laboratory, Berkeley, California 94720, United States

Supporting Information

ABSTRACT: Recent efforts in organic photovoltaics (OPVs) have been devoted to obtaining low-bandgap non-fullerene acceptors (NFAs) for high photocurrent generation. However, the low-lying lowest unoccupied molecular orbital (LUMO) level in narrow bandgap NFAs typically results in a small energy difference (ΔE_{DA}) between the LUMO of the acceptor and the highest occupied molecular orbital (HOMO) of the donor, leading to low open-circuit voltage (V_{OC}). The trade-off between ΔE_{DA} and photocurrent generation significantly limits the simultaneous enhancement of both V_{OC} and short-circuit current density (J_{SC}). Here, we report a new medium-bandgap NFA, IDTT-T, containing a weakly electron-withdrawing *N*-ethyl thiobarbituric acid terminal group on each end of the indacenodithienothiophene (IDTT) core. When paired with a benchmark low-bandgap PTB7-th polymer donor, simultaneous enhancement of both ΔE_{DA} and absorption spectral coverage was realized. The OPV devices yield a V_{OC} of 1.01 V, corresponding to a low energy loss of 0.57 eV in around 10% efficiency single-junction NFA OPVs. The design demonstrates a working principle to concurrently increase ΔE_{DA} and photocurrent generation for high V_{OC} and PCE in bulk fullerene-free heterojunction OPVs.



Bulk heterojunction organic photovoltaics (OPVs) have emerged as a promising class of solar cells that offers a potentially low-cost pathway to large-area, lightweight, and mechanically flexible solar panels.^{1–3} Steady improvement of device performances has been realized over the past decades, partly owing to the great development of active materials, including both the donor⁴ and acceptor materials.^{3,4} Engineering of material properties^{6–8} is crucial to important device parameters, such as short-circuit current (J_{SC}), open-circuit voltage (V_{OC}), fill factor (FF), and the overall power conversion efficiency (PCE), which are related to the absorption in the visible-near-infrared (NIR) spectrum,⁹ relative energy levels,^{10,11} and nanoscale phase morphology¹² of the active materials.^{13–19} The majority of the OPV devices have employed fullerene derivatives as the electron acceptors for their high electron transport property and excellent crystallization behavior.^{13,20,21} Their absorption properties and electronic structures are however less than ideal, which has a limited window for tuning via chemical modification because of the narrow tunability of the fullerene moiety.^{22,23} Very recently,

an emerging class of non-fullerene acceptors (NFAs) based on low-bandgap fused-ring small molecules has rivaled the dominance of fullerene-based acceptors.^{23–31} Their attractive features, such as greater tunability of molecular structures and optoelectronic properties^{32–35} and high PCEs that already surpass that of the best fullerene-based single-junction devices,^{35–42} have re-established the competitiveness of bulk heterojunction OPVs. Since the seminal work by Zhan et al. that demonstrated the use of 3,9-bis(2-methylene-(3-(1,1-dicyanomethylene)-indanone))-5,5,11,11-tetrakis(4-hexylphenyl)-dithieno[2,3-d:2',3'-d']-s-lowindaceno[1,2-b:5,6-b']-dithiophene (ITIC) as a low-bandgap NFA for OPVs,³² great progress has been made in the molecular design of NFAs that enable the fabrication of high-efficiency single-junction devices with PCE over 10%.^{36,43}

Received: March 7, 2018

Accepted: March 27, 2018

63 Despite progress toward approaching the Shockley–Queisser
64 theoretical maximum efficiency, the non-fullerene OPVs still
65 suffer from high energy loss ($\sim 0.7\text{--}1.0$ eV),^{11,15,44,45} which is
66 reflected by the fact that the V_{OC} is generally smaller than half
67 of the optical bandgaps of photoactive molecules in most high-
68 efficiency (PCE $\geq 10\%$) devices.^{11,45} The V_{OC} is a key
69 photovoltaic parameter which is essential to drive portable
70 electronics and consumer electronic devices without employing
71 a complicated tandem structure or resorting to electric
72 utilities.^{26,46–52} In principle, the low V_{OC} primarily results
73 from energy level mismatch or internal energy loss during the
74 photoinduced charge-transfer process.⁵³ The V_{OC} is dependent
75 on the difference between the lowest unoccupied molecular
76 orbital (LUMO) level of the electron acceptor and the highest
77 occupied molecular orbital (HOMO) level of the electron
78 donor ($\Delta E_{DA} = E_{\text{Acceptor}}^{\text{LUMO}} - E_{\text{Donor}}^{\text{HOMO}}$).¹³ For non-fullerene OPVs,
79 much effort has been devoted to reducing the optical bandgaps
80 of non-fullerene acceptors to extend absorption into the near-
81 infrared portion of the solar spectrum for high photocurrent
82 generation.^{33–35,37} This modification generally lowers the
83 LUMO levels, resulting in a decreased ΔE_{DA} and thereby
84 V_{OC} lower than 1 V in most non-fullerene OPVs.^{22,33–35,37,38,54}
85 Such a trade-off between ΔE_{DA} and photocurrent generation
86 limits the simultaneous enhancement of both V_{OC} and J_{SC} for
87 high PCEs in non-fullerene OPVs. The medium-bandgap non-
88 fullerene acceptors, although receiving less attention, are a
89 potential remedy to the trade-off: On one hand, their relatively
90 high-lying LUMO levels can increase ΔE_{DA} for high V_{OC} . On
91 the other hand, high J_{SC} may be realized when combined with a
92 variety of known low-bandgap donors, such as the model
93 polymer PTB7-th, to enhance the absorption spectral coverage.
94 However, to the best of our knowledge, such a design principle
95 has been rarely demonstrated.⁵

96 In this Letter, we demonstrate a proof-of-concept of
97 combining a medium-bandgap non-fullerene acceptor with
98 the low-bandgap donor PTB7-th for high-efficiency OPVs with
99 a high V_{OC} . By adopting an acceptor–donor–acceptor
100 geometry with a weakly electron withdrawing end group, the
101 LUMO energy is increased significantly. This strategy gives rise
102 to an optical bandgap of 2.0 eV that is complementary to
103 electronic energy levels of PTB7-th. The resulting OPVs display
104 a V_{OC} of 1.01 V, which is among the highest in around 10%
105 efficiency single-junction NFA OPVs.

106 In the design of a medium-gap acceptor IDTT-T, the
107 indacenodithienothiophene (IDTT) core of ITIC was retained
108 on account of its proven ability to facilitate phase separation
109 and crystallization while the strongly electron-withdrawing end
110 groups cyano indone of ITIC were replaced with the weakly
111 electron-accepting *N,N'*-diethyl thiobarbituric acid (TBA)
112 (Scheme 1). Molecular modeling based on density function
113 theory (DFT) calculations estimate that this end group
114 substitution would result in a 0.23 eV increase of the optical
115 bandgap and a 0.26 eV increase of the LUMO energy level
116 (Figure 1a). The synthesis of IDTT-T was furnished in 78%
117 yield by refluxing the CHO-terminated IDTT derivative **1** with
118 thiobarbituric acid derivative **2** in the presence of pyridine in
119 CHCl_3 (Scheme 1). The detailed synthesis protocol of IDTT-T
120 acceptor is included in the Supporting Information, and the ^1H
121 NMR and ^{13}C NMR spectra of IDTT-T are shown in Figures
122 S1 and S2, respectively.

123 To understand how the end group and backbone structure
124 affects the orbital energy levels, cyclic voltammetry (CV) was
125 carried out for ITIC and IDTT-T solutions in CHCl_3 using a

Scheme 1. (a) Structural Formulas of Low-Bandgap NFA ITIC and the New Medium-Bandgap NFA IDTT-T, (b) Molecular Structure of the Low-Bandgap Donor Polymer PTB7-th, and (c) Synthetic Scheme of IDTT-T

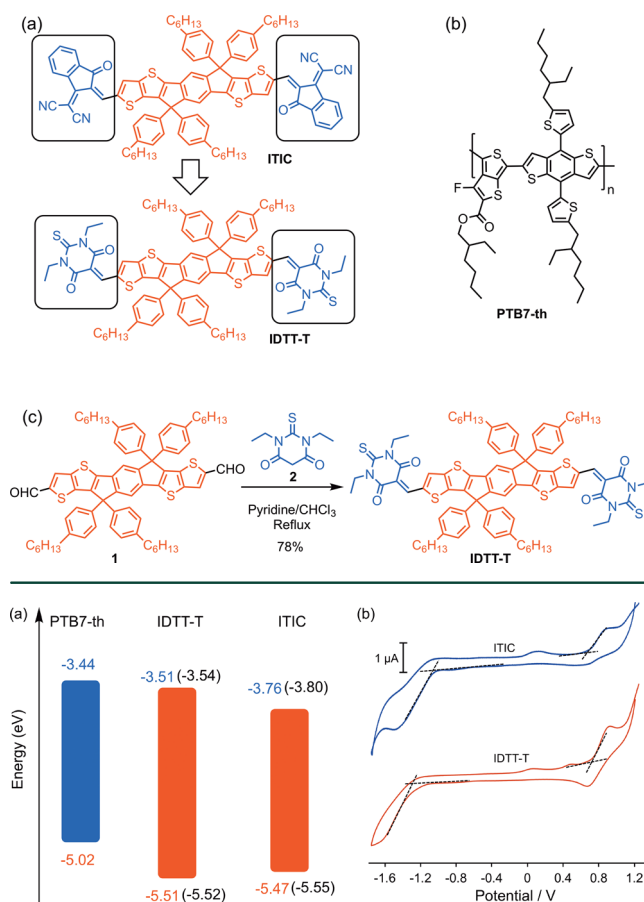


Figure 1. (a) Energy diagram of NFAs and their relative alignment to the energy levels of PTB7-th. The numbers in parentheses are from molecular modeling. (b) CVs of IDTT-T and ITIC (referenced to Fc/Fc^+ redox couple. Scan rate: 100 mV/s).

three-electrode setup and ferrocene as the internal standard.¹²⁶ The ionization potentials and electron affinities, which are also
127 widely termed HOMO and LUMO energy levels, were
128 estimated to be -5.47 and -3.76 eV for ITIC and -5.51 eV
129 and -3.51 eV for IDTT-T, respectively, based on the
130 corresponding onset potential of the first oxidative and
131 reductive wave (Figures 1b and S3 and Table S1). While the
132 variation of HOMO levels was negligible between the two
133 NFAs, the 0.25 eV higher LUMO energy level of IDTT-T
134 compared to ITIC reflected the significantly weaker electron-
135 withdrawing ability of TBA end group than the cyano indone
136 group and is consistent with the modeling results. When
137 combined with the PTB7-th polymer donor,⁵⁵ the ΔE_{DA} shows
138 a significant increase from 1.26 eV for the low-bandgap ITIC
139 acceptor to 1.51 eV for the medium-gap IDTT-T, which alludes
140 to a higher V_{OC} in OPV devices.¹⁴¹

The end group modulation on energy levels correlates well
142 with the absorption properties. As shown in Figure 2a, the
143 absorption edge of IDTT-T shows a significant blue shift of 86
144 nm compared to that of ITIC, in accordance with an optical
145 bandgap increase from 1.71 eV for ITIC to 2.00 eV for IDTT-
146 T. The absorption spectrum of ITIC has a large overlap with 147

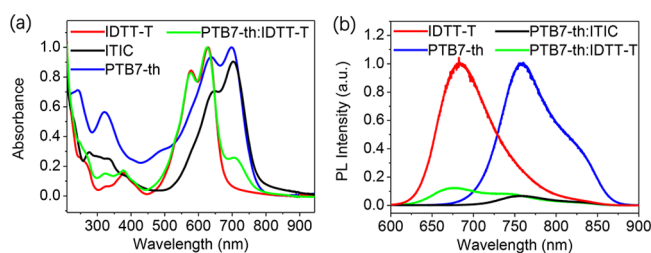


Figure 2. Absorption and photoluminescence spectra of PTB7-th and NFA films: (a) absorption spectra of pristine PTB7-th, ITIC, IDTT-T, and PTB7-th:IDTT-T blend film with a composition ratio of 1:2; (b) photoluminescence spectra of pristine PTB7-th, IDTT-T, PTB7-th:ITIC, and PTB7-th:IDTT-T blend films with a composition ratio of 1:2.

148 that of the donor PTB7-th, leading to incomplete spectral
149 coverage below 635 nm. In contrast, the IDTT-T absorption
150 shows great complementarity to that of PTB7-th and better
151 coverage between 450 and 650 nm, which is advantageous for
152 photocurrent generation. As illustrated in Figure S4, IDTT-T
153 also has a higher extinction coefficient than PTB7-th. It is
154 noteworthy that the LUMO energy level of the TBA-
155 terminated IDTT-T is among the highest for large bandgap
156 NFA featuring similar A–D–A or A– π –D– π –A struc-
157 tures.^{5,47,56–58}

158 Steady-state photoluminescence (PL) spectra of both pristine
159 and PTB7-th:NFA blend films were obtained to examine the
160 PL quenching efficiency, which is related to the exciton
161 dissociation and photoinduced charge-transfer properties of the
162 donor–acceptor pairs. The pristine PTB7-th film exhibited a
163 PL peak at \sim 758 nm (Figure 2b). When blended with IDTT-T
164 in a donor:acceptor ratio of 1:2, the photoluminescence was
165 quenched by \sim 94%. Comparable PL quenching efficiency was
166 observed for the ITIC:PTB7-th blend, indicating similar exciton
167 dissociation in PTB7-th:NFA.⁵⁹ In other words, despite the
168 reduction of the LUMO offset between the donor and acceptor,
169 lifting LUMO energy levels of non-fullerene acceptors to
170 increase ΔE_{DA} has a negligible impact on the charge-transfer
171 efficiency and photocurrent generation. The PTB7-th:IDTT-T
172 film displays an additional PL peak at \sim 675 nm, which should
173 be ascribed to the residual emission of IDTT-T (Figure 2b).

174 Photovoltaic devices based on the inverted structure (ITO/
175 ZnO/PTB7-th:NFA (1:2)/MoO₃/Ag) were fabricated to verify
176 the variation of V_{OC} for different NFAs. As shown in Figure 3a,
177 the prototype PTB7-th:ITIC device displayed a V_{OC} of 0.828 V,
178 a J_{SC} of 14.4 mA/cm², a fill factor (FF) of 67%, and a PCE of
179 8.0%, which are comparable to those of conventional PTB7-
180 th:fullerene-based OPVs.⁶⁰ For the IDTT-T based devices, the

V_{OC} was increased to 1.015 V, together with a FF of 57% and a
181 significantly enhanced J_{SC} of 15.7 mA/cm², leading to a high
182 PCE of 9.0%. Table 1 displays average device parameters for
183 11

Table 1. Average Device Parameters for Two Different NFAs (PTB7-th:ITIC and PTB7-th:IDTT-T) Based Devices

D:A	V_{OC} (V)	J_{SC} (mA/cm ²)	FF (%)	PCE (%)	R_{sc} ^a (Ω)	R_{sh} ^b (Ω)
PTB7-th:ITIC	0.825	14.4	66	7.8	2.3	15.6
PTB7- th:IDTT-T	1.01	15.7	57	9.1	4.9	12.5

^aSeries resistance. ^bShunt resistance.

two different NFAs (PTB7-th:ITIC and PTB7-th:IDTT-T) 184
based devices and shows that the average PCE was around 7.8% 185
and 9.1%, respectively. The devices based on PTB7-th:IDTT-T 186
films exhibited a larger series resistance, which was consistent 187
with the lower FF. The larger series resistance is attributable to 188
a rougher surface [shown later by atomic force microscopy 189
(AFM) characterization] or the presence of more voids for 190
more shorting channels (current-leaking), which is further 191
indicated by the smaller shunt resistance. Further optimization 192
of the film morphology should reduce series resistance and 193
increase shunt resistance for higher FF and better device 194
performance. The high V_{OC} corresponds to a very low energy 195
loss, E_{loss} of 0.57 eV, which was calculated using the equation 196
 $E_{loss} = E_g - eV_{OC}$ ^{61,62} where E_g is the optical bandgap of PTB7- 197
th, the active material with the smallest bandgap. Figure 3b 198
displays external quantum efficiency (EQE) spectra that were 199
acquired from different NFA-based devices. The variation of 200
the calculated J_{SC} by the integration of the EQE spectra with 201
solar spectrum AM 1.5G (100 mW/cm²) is consistent with the 202
variation of the measured J_{SC} . The shift of cutoff edge of EQE 203
curves (Figure 3b) agrees well with the blue shift of the 204
absorption edge of NFA materials (Figure 2a). Significant 205
enhancement between \sim 450 and 650 nm for the PTB7- 206
th:IDTT-T device should be attributed to the characteristic 207
absorption feature from the medium-bandgap IDTT-T, serving 208
as a complementary absorber to that of the low-bandgap PTB7- 209
th polymer donor. 210

Motivated by the superior photovoltaic performance of 211
IDTT-T over ITIC when paired with PTB7-th, further 212
optimization of the PTB7-th:IDTT-T device performance was 213
carried out under various conditions. It was found that thermal 214
annealing treatment of the active layer films resulted in 215
negligible improvement in device performance (Figure S5); 216
therefore, no thermal treatment was exerted in further 217
optimization. A thickness-dependent study of photovoltaic 218
performance in both standard structure (ITO/PEDOT:PSS/ 219
PTB7-th:IDTT-T/Ca/Al) and inverted structure (ITO/ZnO/ 220
PTB7-th:IDTT-T/MoO₃/Ag) devices (Figure 4a,b) indicated 221
that the inverted devices exhibited photovoltaic performance 222
superior to that of the conventional counterparts, consistent 223
with previous reports.^{63,64} For the 57 nm thick PTB7-th:IDTT- 224
T device, the inverted device showed a PCE of 9.1%, whereas 225
the conventional counterpart exhibited only 6.1%. Additionally, 226
the V_{OC} of 1.01 V in the inverted device was higher than the 227
 V_{OC} of 0.888 V in the conventional counterpart. However, the 228
thicker active layer (e.g., 78 and 110 nm) led to decrease in 229
photovoltaic performance in both conventional and inverted 230
devices. With the optimal thickness of 57 nm, we subsequently 231
carried out the study of photovoltaic performance as a function 232

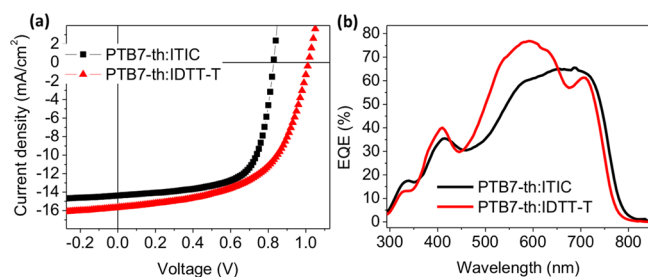


Figure 3. Photovoltaic performance for two different NFAs (PTB7-th:ITIC and PTB7-th:IDTT-T) based devices: (a) J – V curves under illumination of 100 mW/cm², AM 1.5G; (b) EQE curves.

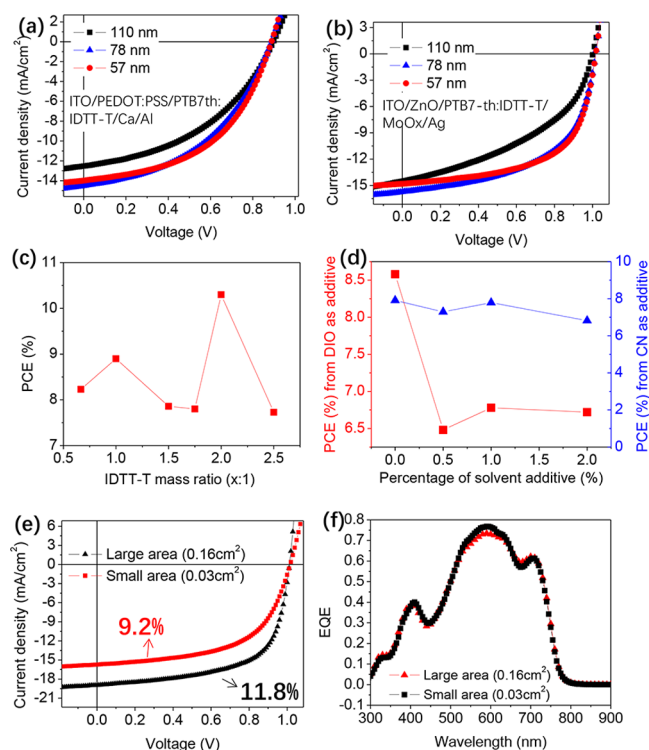


Figure 4. Optimization of photovoltaic performances: J - V curves acquired from devices based on the PTB7-th:IDTT-T active layer in (a) conventional structure (ITO/PEDOT:PSS/PTB7-th:IDTT-T/Ca/Al) and (b) inverted structure (ITO/ZnO/PTB7-th:IDTT-T/MoOx/Ag) device; variation in PCE as a function of (c) composition ratio between IDTT-T and PTB7-th; and (d) percentage of solvent additives [blue triangles, chloronaphthalene (CN); red squares, 1,8-diiodooctane (DIO)]; (e) J - V curves of the highest-performance cells with different device areas under illumination of 100 mW/cm²; (f) corresponding EQE curves for devices in panel e.

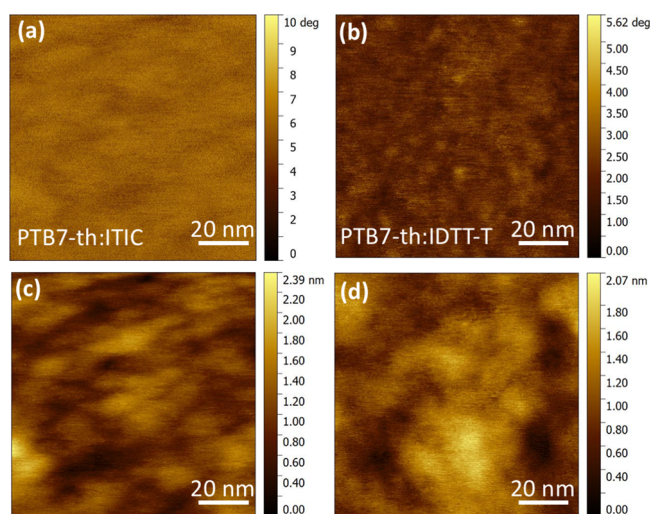


Figure 5. Atomic force microscopic (AFM) phase (a and b) and amplitude (c and d) images of PTB7-th:ITIC (a and c) and PTB7-th:IDTT-T (b and d) blend films with a composition ratio of 1:2.

AFM cantilever.¹¹ For the PTB7-th:IDTT-T (Figure 5b) film, the obviously improved phase contrast of the donor and acceptor domains indicates the enhanced phase separation that is beneficial for improved exciton dissociation and photo-induced charge transfer.

Grazing incident wide-angle X-ray scattering (GIWAXS) studies were conducted to further reveal the molecular packing behavior in the thin films of individual components and the blends. The ITIC (Figure 6a) and IDTT-T (Figure 6b) films displayed varying degrees of crystallinity in the horizontal (100) plane, with the former showing a more discernible (010) out-of-plane diffraction peak that suggests “face-on” oriented crystallites. The GIWAXS pattern of PTB7-th (Figure 6c) signified that the PTB7-th polymers form crystallites with a preferred face-on orientation. In the two blended polymer:NFA films (Figure 6d,e), the preferential “face-on” orientations of the PTB7-th polymer donor was maintained, meanwhile both the in-plane peaks and the out-of-plane peaks of the NFAs disappeared, as can be seen from the vertical and horizontal linecuts (Figure 6g,h). The decreased crystallinity was in accordance with good blending between the polymer and the NFA small molecules, a prerequisite for the formation of favorable phase separation at the nanoscale for efficient charge separation.⁷⁰ The very similar patterns for the ITIC and IDTT-T blend films also suggested that the end groups in NFAs have little impact on molecular orientation and packing behavior, thus implying that the thin film morphology does not account for the simultaneous enhancement of both V_{OC} and J_{SC} . In addition, thermal annealing of the PTB7-th:IDTT-T film induced no notable changes of the GIWAXS pattern (Figure 6f), which suggests that the nanoscale morphology was thermally stable under such conditions. This thermal behavior agrees well with the observation of very similar device performances before and after thermal treatment, which also indicates good device stability.

In order to understand how the end groups in NFAs impact charge transport properties, the space charge limited current (SCLC) method was applied to estimate electron and hole mobilities in the PTB7-th:ITIC and PTB7-th:IDTT-T blend films. The J - V curves (measured in the dark) of both electron-only and hole-only devices are shown in Figure S7. By fitting

of IDTT-T:PTB7-th composition ratio in the active layer. It was found that the devices with a donor:acceptor ratio of 1:2 showed the highest PCE of 10.3% (Figure 4c). The solvent additives, such as chloronaphthalene (CN) and 1,8-diiodooctane (DIO), played a negative effect to give decreased PCE (Figure 4d), which is different from previously reported results.^{14,65–67} Considering the above optimal fabrication conditions, we fabricated both large-area (0.16 cm²) and small-area (0.03 cm²) devices, which yielded the highest PCEs of 9.2% and 11.8% with V_{OC} s of 1.01 V, respectively (Figure 4e). A histogram of the device efficiencies is plotted in Figure S6. The variation in J_{SC} values for different device areas is consistent with the variation in the calculated J_{SC} based on the EQE curves (Figure 4f). The high V_{OC} of over 1 V in our devices is among the highest for high-efficiency (over 10%) NFA OPVs.^{68,69}

The AFM phase and amplitude images were obtained to examine nanoscale phase morphology in the blend films of PTB7-th:ITIC (Figure 5a,c) and PTB7-th:IDTT-T (Figure 5b,d). The amplitude images show similar surface roughness of 0.230 and 0.300 nm for PTB7-th:ITIC (Figure 5c) and PTB7-th:IDTT-T (Figure 5d), respectively. The phase contrast between PTB7-th and ITIC domains is invisible for the PTB7-th:ITIC blend film (Figure 5a), most likely because of the similar elastic properties of PTB7-th and ITIC materials, leading to the similar phase angle change with respect to the

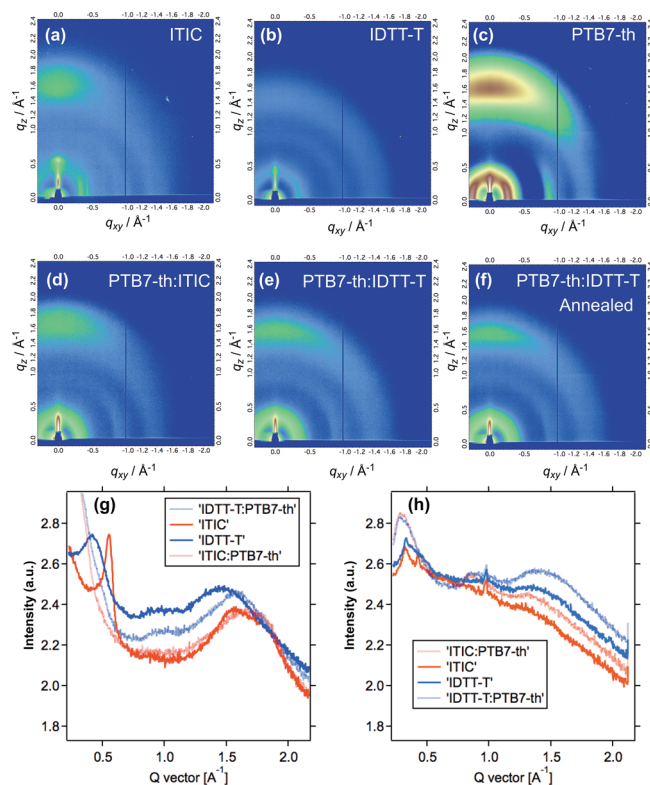


Figure 6. 2D GIWAXS patterns of pristine films (a) ITIC, (b) IDTT-T, and (c) PTB7-th and blend films (d) PTB7-th:ITIC, (e) PTB7-th:IDTT-T, and (f) PTB7-th:IDTT-T (thermally annealed at 100 °C for 10 min). (g) Vertical and (h) horizontal linecuts of the pure NFA films and their blends with PTB7-th.

the $J-V$ curves with the SCLC model,^{71,72} we found that the electron and hole mobilities of the PTB7-th:ITIC blend film were 2.43×10^{-4} and 2.07×10^{-2} $\text{cm}^2/(\text{V s})$ (Table 2),

Table 2. Electron and Hole Mobilities in PTB7-th:ITIC and PTB7-th:IDTT-T Blend Films Estimated by the Space Charge Limited Current (SCLC) Method

material	μ_e ($\text{cm}^2/(\text{V s})$)	μ_h ($\text{cm}^2/(\text{V s})$)
PTB7-th:ITIC	2.43×10^{-4}	2.07×10^{-2}
PTB7-th:IDTT-T	3.98×10^{-3}	5.19×10^{-3}

respectively. When using end-group-modified IDTT-T to replace ITIC in the blend films, the electron and hole mobilities of the blend film were determined to be 3.98×10^{-3} and 5.19×10^{-3} $\text{cm}^2/(\text{V s})$, respectively, showing not only an increased electron mobility but also clearly more balanced electron and hole transport than those of the PTB7-th:ITIC blend film. Balanced carrier transport is important for reducing bimolecular recombination and also improves charge collection at the respective electrodes. As a result, J_{SC} was considerably improved in the corresponding devices (Figure 3a).

We present a high-performance medium-bandgap non-fullerene acceptor that features an optical bandgap of 2.0 eV and a high LUMO energy level. The combined use of a weakly electron-withdrawing TBA end group and the IDTT core in an A–D–A geometry gives rise to IDTT-T with a significantly raised LUMO energy level compared to ITIC, together with absorption in the blue region of the visible spectrum that 20 matches well with that of the low-bandgap PTB7-th donor.

Because of the high LUMO level and the complementary absorption properties, the OPV devices using PTB7-th:IDTT-T as the active layer showcase a high V_{OC} over 1 V, together with a high J_{SC} low energy loss, and a highest PCE reaching 11.8% in lab-scale devices. This performance compares favorably to the performance of other wider gap NFAs reported to-date (Table S2).^{15–18} While the current OPV devices with leading efficiencies are still based on low-bandgap NFAs,^{36,43} which feature high photocurrent generation but often at the expense of V_{OC} , this work demonstrated that simultaneous increase of V_{OC} and photocurrent generation in bulk heterojunction OPVs can be realized by the use of judiciously designed wide bandgap NFAs and donor materials with proper spectrum overlap. The discovery of potent wide bandgap NFAs thus not only broadens the scope of the OPV material design landscape but also opens the door to high-efficiency OPV devices in new applications, such as multicomponent solar cells.

EXPERIMENTAL SECTION

Synthesis of ZnO. The ZnO nanoparticles were synthesized by a sol–gel method, modified from the procedure reported in the literature.⁷³ In a 20 mL vial, potassium hydroxide (94.4 mg, 1.7 mmol) was first dissolved in ethanol (10 mL); the solution was then sonicated and cooled to 0 °C using an ice bath. In a second 20 mL vial, zinc acetate dihydrate (220 mg, 1 mmol) was dissolved in ethanol (10 mL); the solution was then heated to 70 °C for up to 30 min or until all the zinc acetate dihydrate dissolved. Heating beyond the recommended time leads to precipitation of insoluble zinc acetate and should be avoided. Upon dissolution, the ZnAc solution was taken off the heat and then cooled at 0 °C for about a minute. The KOH solution was subsequently added into the ZnAc solution dropwise with stirring. The resulting clear solution was stored in a refrigerator overnight. The clear zinc oxide solution was transferred into two large falcon tubes. Zinc oxide nanoparticles were precipitated by adding hexanes (40 mL) in each tube followed by centrifuging for 15 min at 4000 rpm. The solution was decanted off, and the remaining ZnO pellet was redissolved in ethanol (10 mL) for further use.

Thin Film and Device Characterization. The $J-V$ curves were acquired in the dark and under illumination of one sun (AM 1.5G) with light intensity of 100 mW/cm^2 . A standard Newport silicon diode was applied to calibrate the light intensity. EQE was measured by a home-built IPCE system. The absorption spectrum and photoluminescence spectrum were obtained by a Cary 5000 UV-vis-NIR spectrometer and a Horiba NanoLog spectrofluorometer, respectively. The excitation wavelength for PL measurement was 500 nm. An Asylum MFP-3D stand-alone AFM instrument from Oxford Instruments was used to take AFM images under tapping mode. GIWAXS patterns were acquired under X-ray incident angle of 0.14° and X-ray energy of 10 keV at Beamline 7.3.3 of the Advanced Light Source, Lawrence Berkeley National Laboratory.

Device Fabrication and Characterization. For the inverted device fabrication, the ZnO nanoparticle solution, filtered by a 0.25 μm filter, was spun-cast at 4000 rpm for 60 s on a clean ITO glass substrate and thermally annealed at 120 °C for 10 min in air. The concentration of the PTB7-th:NFA (composition ratio = 1:2) solution was 25 mg/mL , dissolved in chlorobenzene. The solution was spun-coated on the ZnO layer at 3000 rpm for 40 s in a N_2 -filled glovebox. The 8 nm thick MoO_3 and 100 nm thick Ag layers were subsequently prepared by thermal evaporation. For the standard device

383 fabrication, the active layer fabrication was the same as that for
384 the inverted device, and the only differences were (1) the hole
385 transport layer PEDOT:PSS (P4083), which was spun-coated
386 on ITO glass at 4000 rpm followed by a thermal annealing
387 treatment of 135 °C for 20 min, and (2) the cathode calcium
388 (20 nm) and aluminum (100 nm) prepared by thermal
389 evaporation under vacuum condition (2×10^{-6} mbar). Both
390 large-area (0.16 cm²) and small-area (0.03 cm²) devices were
391 fabricated.

392 ■ ASSOCIATED CONTENT

393 ● Supporting Information

394 The Supporting Information is available free of charge on the
395 ACS Publications website at DOI: 10.1021/acsenery-
396 lett.8b00366.

397 Synthesis details and additional optical, electrochemical,
398 and device characterization data (PDF)

399 ■ AUTHOR INFORMATION

400 Corresponding Authors

401 *E-mail: yliu@lbl.gov.

402 *E-mail: yangb1@hnu.edu.cn.

403 ORCID

404 Bo He: 0000-0003-1444-4625

405 Yi Liu: 0000-0002-3954-6102

406 Author Contributions

407 [‡]B.H. and B.Y. contributed equally.

408 Notes

409 The authors declare no competing financial interest.

410 ■ ACKNOWLEDGMENTS

411 This work was performed at the Molecular Foundry, and the X-
412 ray experiments were conducted at the Advanced Light Source
413 (ALS), Lawrence Berkeley National Laboratory, all of which are
414 supported by the Office of Science, Office of Basic Energy
415 Sciences, of the U.S. Department of Energy under Contract No.
416 DE-AC02-05CH11231.

417 ■ REFERENCES

- 418 (1) Li, G.; Shrotriya, V.; Huang, J.; Yao, Y.; Moriarty, T.; Emery, K.;
419 Yang, Y. High-Efficiency Solution Processable Polymer Photovoltaic
420 Cells by Self-Organization of Polymer Blends. *Nat. Mater.* **2005**, *4*,
421 864–868.
- 422 (2) Shaheen, S. E.; Brabec, C. J.; Sariciftci, N. S.; Padinger, F.;
423 Fromherz, T.; Hummelen, J. C. 2.5% Efficient Organic Plastic Solar
424 Cells. *Appl. Phys. Lett.* **2001**, *78*, 841–843.
- 425 (3) Heeger, A. J. 25th Anniversary Article: Bulk Heterojunction Solar
426 Cells: Understanding the Mechanism of Operation. *Adv. Mater.* **2014**,
427 *26*, 10–28.
- 428 (4) Cheng, Y. J.; Yang, S. H.; Hsu, C. S. Synthesis of Conjugated
429 Polymers for Organic Solar Cell Applications. *Chem. Rev.* **2009**, *109*,
430 5868–5923.
- 431 (5) Chen, W.; Zhang, Q. Recent Progress in Non-Fullerene Small
432 Molecule Acceptors in Organic Solar Cells (OSCs). *J. Mater. Chem. C*
433 **2017**, *5*, 1275–1302.
- 434 (6) He, Z.; Zhong, C.; Huang, X.; Wong, W. Y.; Wu, H.; Chen, L.;
435 Su, S.; Cao, Y. Simultaneous Enhancement of Open-Circuit Voltage,
436 Short-Circuit Current Density, and Fill Factor in Polymer Solar Cells.
437 *Adv. Mater.* **2011**, *23*, 4636–4643.
- 438 (7) Elumalai, N. K.; Uddin, A. Open Circuit Voltage of Organic Solar
439 Cells: an In-Depth Review. *Energy Environ. Sci.* **2016**, *9*, 391–410.
- 440 (8) Eckstein, B. J.; Melkonyan, F. S.; Zhou, N.; Manley, E. F.; Smith,
441 J.; Timalina, A.; Chang, R. P. H.; Chen, L. X.; Facchetti, A.; Marks, T.

- J. Buta-1,3-diyne-Based π -Conjugated Polymers for Organic Tran- 442
sistors and Solar Cells. *Macromolecules* **2017**, *50*, 1430–1441. 443
- (9) Liu, J.; Liu, F.; Ding, Z.; Wang, L. An Organoboron Compound 444
with Wide Absorption Spectrum for Organic Solar Cell Application. 445
Chem. Commun. **2017**, *53*, 12213–12216. 446
- (10) Yang, B.; Yuan, Y.; Sharma, P.; Poddar, S.; Korlacki, R.; 447
Ducharme, S.; Gruverman, A.; Saraf, R.; Huang, J. Tuning the Energy 448
Level Offset between Donor and Acceptor with Ferroelectric Dipole 449
Layers for Increased Efficiency in Bilayer Organic Photovoltaic Cells. 450
Adv. Mater. **2012**, *24*, 1455–1460. 451
- (11) Wang, G.; Eastham, N. D.; Aldrich, T. J.; Ma, B.; Manley, E. F.; 452
Chen, Z.; Chen, L.; Olvera, M.; Chang, R.; Melkonyan, F.; et al. 453
Photoactive Blend Morphology Engineering through Systematically 454
Tuning Aggregation in All-Polymer Solar Cells. *Adv. Energy Mater.* 455
2018, 1702173. 456
- (12) Kwon, O. K.; Uddin, M. A.; Park, J. H.; Park, S. K.; Nguyen, T. 457
L.; Woo, H. Y.; Park, S. Y. A High Efficiency Nonfullerene Organic 458
Solar Cell with Optimized Crystalline Organizations. *Adv. Mater.* **2016**, 459
28, 910–916. 460
- (13) Blom, P. W. M.; Mihailetchi, V. D.; Koster, L. J. A.; Markov, D. 461
E. Device Physics of Polymer:Fullerene Bulk Heterojunction Solar 462
Cells. *Adv. Mater.* **2007**, *19*, 1551–1566. 463
- (14) Perez, L. A.; Rogers, J. T.; Brady, M. A.; Sun, Y.; Welch, G. C.; 464
Schmidt, K.; Toney, M. F.; Jinnai, H.; Heeger, A. J.; Chabinyc, M. L.; 465
et al. The Role of Solvent Additive Processing in High Performance 466
Small Molecule Solar Cells. *Chem. Mater.* **2014**, *26*, 6531–6541. 467
- (15) Tang, A.; Xiao, B.; Wang, Y.; Gao, F.; Tajima, K.; Bin, H.; 468
Zhang, Z.-G.; Li, Y.; Wei, Z.; Zhou, E. Simultaneously Achieved High 469
Open-Circuit Voltage and Efficient Charge Generation by Fine- 470
Tuning Charge-Transfer Driving Force in Nonfullerene Polymer Solar 471
Cells. *Adv. Funct. Mater.* **2018**, *28*, 1704507. 472
- (16) Liu, Y.; Zhang, Z.; Feng, S. Y.; Li, M.; Wu, L. L.; Hou, R.; Xu, X. 473
J.; Chen, X. B.; Bo, Z. S. Exploiting Noncovalently Conformational 474
Locking as a Design Strategy for High Performance Fused-Ring 475
Electron Acceptor Used in Polymer Solar Cells. *J. Am. Chem. Soc.* 476
2017, *139*, 3356–3359. 477
- (17) Hendsbee, A.; Sun, J.; Law, W.; Yan, H.; Hill, I.; Spasyuk, D.; 478
Welch, G. Synthesis, Self-Assembly, and Solar Cell Performance of *N*- 479
Annulated Perylene Diimide Non-Fullerene Acceptors. *Chem. Mater.* 480
2016, *28*, 7098–7109. 481
- (18) Baran, D.; Ashraf, R. S.; Hanifi, D. A.; Abdelsamie, M.; 482
Gasparini, N.; Röhr, J. A.; Holliday, S.; Wadsworth, A.; Lockett, S.; 483
Neophytou, M.; et al. Reducing the Efficiency-Stability-Cost Gap of 484
Organic Photovoltaics with Highly Efficient and Stable Small Molecule 485
Acceptor Ternary Solar Cells. *Nat. Mater.* **2017**, *16*, 363–369. 486
- (19) Aldrich, T. J.; Swick, S. M.; Melkonyan, F. S.; Marks, T. J. 487
Enhancing Indacenodithiophene Acceptor Crystallinity via Substituent 488
Manipulation Increases Organic Solar Cell Efficiency. *Chem. Mater.* 489
2017, *29*, 10294–10298. 490
- (20) Heumueller, T.; Mateker, W. R.; Distler, A.; Fritze, U. F.; 491
Checharoen, R.; Nguyen, W. H.; Biele, M.; Salvador, M.; Delius, M. 492
V.; Egelhaaf, H. J. Morphological and Electrical Control of Fullerene 493
Dimerization Determines Organic Photovoltaic Stability. *Energy* 494
Environ. Sci. **2016**, *9*, 247–256. 495
- (21) Li, Y. Fullerene-Bisadduct Acceptors for Polymer Solar Cells. 496
Chem. - Asian J. **2013**, *8*, 2316–2328. 497
- (22) Zhao, W.; Qian, D.; Zhang, S.; Li, S.; Inganäs, O.; Gao, F.; Hou, 498
J. Fullerene-Free Polymer Solar Cells with over 11% Efficiency and 499
Excellent Thermal Stability. *Adv. Mater.* **2016**, *28*, 4734–4739. 500
- (23) Zhang, X.; Lu, Z.; Ye, L.; Zhan, C.; Hou, J.; Zhang, S.; Jiang, B.; 501
Zhao, Y.; Huang, J.; Zhang, S. A Potential Perylene Diimide Dimer- 502
Based Acceptor Material for Highly Efficient Solution-Processed 503
Non-Fullerene Organic Solar Cells with 4.03% Efficiency. *Adv. Mater.* 504
2013, *25*, 5791–5797. 505
- (24) Lin, Y.; Wang, J.; Zhang, Z. G.; Bai, H.; Li, Y.; Zhu, D.; Zhan, X. 506
An Electron Acceptor Challenging Fullerenes for Efficient Polymer 507
Solar Cells. *Adv. Mater.* **2015**, *27*, 1170–1174. 508
- (25) Wu, Q.; Zhao, D.; Yang, J.; Sharapov, V.; Cai, Z.; Li, L.; Zhang, 509
N.; Neshchadin, A.; Chen, W.; Yu, L. Propeller-Shaped Acceptors for 510

- 511 High-Performance Non-Fullerene Solar Cells: Importance of Molec-
512 ular Geometry Rigidity. *Chem. Mater.* **2017**, *29*, 1127–1133.
- 513 (26) Wang, Y.; Fan, Q.; Guo, X.; Li, W.; Guo, B.; Su, W.; Ou, X.;
514 Zhang, M. High-Performance Nonfullerene Polymer Solar Cells Based
515 on Fluorinated Wide Bandgap Copolymer with a High Open-Circuit
516 Voltage of 1.04 V. *J. Mater. Chem. A* **2017**, *5*, 22180–22185.
- 517 (27) Hartnett, P. E.; Matte, H. S. S. R.; Eastham, N. D.; Jackson, N.
518 E.; Wu, Y. L.; Chen, L. X.; Ratner, M. A.; Chang, R. P. H.; Hersam, M.
519 C.; Wasielewski, M. R.; et al. Ring-Fusion as a Perylenediimide Dimer
520 Design Concept for High-Performance Non-Fullerene Organic
521 Photovoltaic Acceptors. *Chem. Sci.* **2016**, *7*, 3543–3555.
- 522 (28) McAfee, S. M.; Dayneko, S. V.; Josse, P.; Blanchard, P.;
523 Cabanetos, C.; Welch, G. C. Simply Complex: The Efficient Synthesis
524 of an Intricate Molecular Acceptor for High-Performance Air-
525 Processed and Air-Tested Fullerene-Free Organic Solar Cells. *Chem.*
526 *Mater.* **2017**, *29*, 1309–1314.
- 527 (29) Zhong, H.; Wu, C. H.; Li, C. Z.; Carpenter, J.; Chueh, C. C.;
528 Chen, J. Y.; Ade, H.; Jen, A. K. Rigidifying Nonplanar Perylene
529 Diimides by Ring Fusion Toward Geometry-Tunable Acceptors for
530 High-Performance Fullerene-Free Solar Cells. *Adv. Mater.* **2016**, *28*,
531 951–958.
- 532 (30) Lin, Y. Z.; Wang, J. Y.; Dai, S. X.; Li, Y. F.; Zhu, D. B.; Zhan, X.
533 W. A Twisted Dimeric Perylene Diimide Electron Acceptor for
534 Efficient Organic Solar Cells. *Adv. Energy Mater.* **2014**, *4*, 1400420.
- 535 (31) Fei, Z.; Eisner, F. D.; Jiao, X.; Azzouzi, M.; Röhr, J. A.; Han, Y.;
536 Shahid, M.; Chesman, A. R.; Easton, C. D.; McNeill, C. R.; et al. An
537 Alkylated Indacenodithieno [3,2-b]Thiophene-Based Nonfullerene
538 Acceptor with High Crystallinity Exhibiting Single Junction Solar
539 Cell Efficiencies Greater than 13% with Low Voltage Losses. *Adv.*
540 *Mater.* **2018**, *30*, 1705209.
- 541 (32) Lin, Y.; Wang, J.; Zhang, Z.-G.; Bai, H.; Li, Y.; Zhu, D.; Zhan, X.
542 An Electron Acceptor Challenging Fullerenes for Efficient Polymer
543 Solar Cells. *Adv. Mater.* **2015**, *27*, 1170–1174.
- 544 (33) Lin, Y.; He, Q.; Zhao, F.; Huo, L.; Mai, J.; Lu, X.; Su, C.-J.; Li,
545 T.; Wang, J.; Zhu, J.; Sun, Y.; Wang, C.; Zhan, X. A Facile Planar
546 Fused-Ring Electron Acceptor for as-Cast Polymer Solar Cells with
547 8.71% Efficiency. *J. Am. Chem. Soc.* **2016**, *138*, 2973–2976.
- 548 (34) Lin, Y.; Zhao, F.; He, Q.; Huo, L.; Wu, Y.; Parker, T. C.; Ma,
549 W.; Sun, Y.; Wang, C.; Zhu, D.; Heeger, A. J.; Marder, S. R.; Zhan, X.
550 High-Performance Electron Acceptor with Thienyl Side Chains for
551 Organic Photovoltaics. *J. Am. Chem. Soc.* **2016**, *138*, 4955–4961.
- 552 (35) Li, Y.; Zhong, L.; Gautam, B.; Bin, H.-J.; Lin, J.-D.; Wu, F.-P.;
553 Zhang, Z.; Jiang, Z.-Q.; Zhang, Z.-G.; Gundogdu, K.; Li, Y.; Liao, L.-S.
554 A Near-Infrared Non-Fullerene Electron Acceptor for High Perform-
555 ance Polymer Solar Cells. *Energy Environ. Sci.* **2017**, *10*, 1610–1620.
- 556 (36) Zhao, W.; Li, S.; Yao, H.; Zhang, S.; Zhang, Y.; Yang, B.; Hou, J.
557 Molecular Optimization Enables over 13% Efficiency in Organic Solar
558 Cells. *J. Am. Chem. Soc.* **2017**, *139*, 7148–7151.
- 559 (37) Cui, Y.; Yao, H.; Gao, B.; Qin, Y.; Zhang, S.; Yang, B.; He, C.;
560 Xu, B.; Hou, J. Fine-Tuned Photoactive and Interconnection Layers
561 for Achieving over 13% Efficiency in a Fullerene-Free Tandem
562 Organic Solar Cell. *J. Am. Chem. Soc.* **2017**, *139*, 7302–7309.
- 563 (38) Xue, L.; Yang, Y.; Xu, J.; Zhang, C.; Bin, H.; Zhang, Z.-G.; Qiu,
564 B.; Li, X.; Sun, C.; Gao, L.; Yao, J.; Chen, X.; Yang, Y.; Xiao, M.; Li, Y.
565 Side Chain Engineering on Medium Bandgap Copolymers to Suppress
566 Triplet Formation for High-Efficiency Polymer Solar Cells. *Adv. Mater.*
567 **2017**, *29*, 1703344.
- 568 (39) Liu, T.; Meng, D.; Cai, Y.; Sun, X.; Li, Y.; Huo, L.; Liu, F.;
569 Wang, Z.; Russell, T. P.; Sun, Y. High-Performance Non-Fullerene
570 Organic Solar Cells Based on a Selenium-Containing Polymer Donor
571 and a Twisted Perylene Bisimide Acceptor. *Adv. Sci.* **2016**, *3*, 1600117.
- 572 (40) McAfee, S. M.; Payne, A.; Dayneko, S. V.; Kini, G. P.; Song, C.
573 E.; Lee, J.; Welch, G. C. A Non-Fullerene Acceptor with a Diagnostic
574 Morphological Handle for Streamlined Screening of Donor Materials
575 in Organic Solar Cells. *J. Mater. Chem. A* **2017**, *5*, 16907–16913.
- 576 (41) Kim, T.; Kim, J. H.; Kang, T. E.; Lee, C.; Kang, H.; Shin, M.;
577 Wang, C.; Ma, B.; Jeong, U.; Kim, T. S.; et al. Flexible, Highly Efficient
578 All-Polymer Solar Cells. *Nat. Commun.* **2015**, *6*, 8547.
- (42) Sun, D.; Meng, D.; Cai, Y.; Fan, B.; Li, Y.; Jiang, W.; Huo, L.; 579
Sun, Y.; Wang, Z. Non-Fullerene-Acceptor-Based Bulk-Heterojunction 580
Organic Solar Cells with Efficiency over 7. *J. Am. Chem. Soc.* **2015**, *137*, 581
11156–11162. 582
- (43) Xiao, Z.; Jia, X.; Ding, L. Ternary Organic Solar Cells Offer 14% 583
Power Conversion Efficiency. *Sci. Bull.* **2017**, *62*, 1562–1564. 584
- (44) Wang, M.; Wang, H.; Yokoyama, T.; Liu, X.; Huang, Y.; Zhang, 585
Y.; Nguyen, T.-Q.; Aramaki, S.; Bazan, G. C. High Open Circuit 586
Voltage in Regioregular Narrow Band Gap Polymer Solar Cells. *J. Am.* 587
Chem. Soc. **2014**, *136*, 12576–12579. 588
- (45) Yang, B.; Guo, F.; Yuan, Y.; Xiao, Z.; Lu, Y.; Dong, Q.; Huang, J. 589
Solution-Processed Fullerene-Based Organic Schottky Junction 590
Devices for Large-Open-Circuit-Voltage Organic Solar Cells. *Adv.* 591
Mater. **2013**, *25*, 572–577. 592
- (46) Sullivan, P.; Schumann, S.; Da Campo, R.; Howells, T.; Duraud, 593
A.; Shipman, M.; Hatton, R. A.; Jones, T. S. Ultra-High Voltage 594
Multijunction Organic Solar Cells for Low-Power Electronic 595
Applications. *Adv. Energy Mater.* **2013**, *3*, 239–244. 596
- (47) Beaumont, N.; Cho, S. W.; Sullivan, P.; Newby, D.; Smith, K. E.; 597
Jones, T. S. Boron Subphthalocyanine Chloride as an Electron 598
Acceptor for High-Voltage Fullerene-Free Organic Photovoltaics. *Adv.* 599
Funct. Mater. **2012**, *22*, 561–566. 600
- (48) Ma, D.; Feng, S.; Zhang, J.; Kou, C.; Gong, X.; Li, Q.; Xu, X.; 601
Yan, S.; Bo, Z. Non-Fullerene Small Molecular Acceptors with a 602
Carbazole Core for Organic Solar Cells with High Open-Circuit 603
Voltage. *Dyes Pigm.* **2017**, *146*, 293–299. 604
- (49) Zhang, Y.; Guo, X.; Guo, B.; Su, W.; Zhang, M.; Li, Y. 605
Nonfullerene Polymer Solar Cells Based on a Perylene Monoimide 606
Acceptor with a High Open-Circuit Voltage of 1.3 V. *Adv. Funct.* 607
Mater. **2017**, *27*, 1603892. 608
- (50) Cheng, P.; Zhang, M.; Lau, T. K.; Wu, Y.; Jia, B.; Wang, J.; Yan, 609
C.; Qin, M.; Lu, X.; Zhan, X. Realizing Small Energy Loss of 0.55 eV, 610
High Open-Circuit Voltage > 1 V and High Efficiency > 10% in 611
Fullerene-Free Polymer Solar Cells via Energy Driver. *Adv. Mater.* 612
2017, *29*, 1605216. 613
- (51) Li, S.; Liu, W.; Li, C. Z.; Lau, T. K.; Lu, X.; Shi, M.; Chen, H. A 614
Non-Fullerene Acceptor with a Fully Fused Backbone For Efficient 615
Polymer Solar Cells with a High Open-Circuit Voltage. *J. Mater. Chem.* 616
A **2016**, *4*, 14983–14987. 617
- (52) Sun, J.; Zhang, Z.; Yin, X.; Zhou, J.; Yang, L.; Geng, R.; Zhang, 618
F.; Zhu, R.; Yu, J.; Tang, W. High Performance Non-Fullerene 619
Polymer Solar Cells Based on PTB7-Th as the Electron Donor with 620
10.42% Efficiency. *J. Mater. Chem. A* **2018**, *6*, 2549–2554. 621
- (53) Liu, J.; Chen, S.; Qian, D.; Gautam, B.; Yang, G.; Zhao, J.; 622
Bergqvist, J.; Zhang, F.; Ma, W.; Ade, H.; Ingañäs, O.; Gundogdu, K.; 623
Gao, F.; Yan, H. Fast Charge Separation in a Non-Fullerene Organic 624
Solar Cell with a Small Driving Force. *Nat. Energy* **2016**, *1*, 16089. 625
- (54) Ye, L.; Sun, K.; Jiang, W.; Zhang, S.; Zhao, W.; Yao, H.; Wang, 626
Z.; Hou, J. Enhanced Efficiency in Fullerene-Free Polymer Solar Cell 627
by Incorporating Fine-designed Donor and Acceptor Materials. *ACS* 628
Appl. Mater. Interfaces **2015**, *7*, 9274–9280. 629
- (55) Ding, Z.; Long, X.; Dou, C.; Liu, J.; Wang, L. A Polymer 630
Acceptor with an Optimal LUMO Energy Level for All-Polymer Solar 631
Cells. *Chem. Sci.* **2016**, *7*, 6197–6202. 632
- (56) Li, Z.; Jiang, K.; Yang, G.; Lai, J. Y. L.; Ma, T.; Zhao, J.; Ma, W.; 633
Yan, H. Donor Polymer Design Enables Efficient Non-Fullerene 634
Organic Solar Cells. *Nat. Commun.* **2016**, *7*, 13094. 635
- (57) Wen, S.; Wu, Y.; Wang, Y.; Li, Y.; Liu, L.; Jiang, H.; Liu, Z.; 636
Yang, R. Pyran-Bridged Indacenodithiophene: A Novel Building Block 637
for Constructing Efficient A-D-A Type Nonfullerene Acceptor for 638
Polymer Solar Cells. *ChemSusChem* **2018**, *11*, 360–366. 639
- (58) Lim, E. Two A–D–A-Type Non-Fullerene Small Molecule 640
Acceptors Based on 1,3-Dimethylbarbituric Acid for OPVs. *B. Kor.* 641
Chem. Soc. **2017**, *38*, 285–288. 642
- (59) Clarke, T. M.; Ballantyne, A.; Shoaee, S.; Ying, W. S.; Duffy, W.; 643
Heeney, M.; McCulloch, I.; Nelson, J.; Durrant, J. R. Analysis of Charge 644
Photogeneration as a Key Determinant of Photocurrent Density in 645
Polymer: Fullerene Solar Cells. *Adv. Mater.* **2010**, *22*, 5287–5291. 646

- 647 (60) Liao, S.-H.; Jhuo, H.-J.; Cheng, Y.-S.; Chen, S.-A. Fullerene
648 Derivative-Doped Zinc Oxide Nanofilm as the Cathode of Inverted
649 Polymer Solar Cells with Low-Bandgap Polymer (PTB7-Th) for High
650 Performance. *Adv. Mater.* **2013**, *25*, 4766–4771.
- 651 (61) Ran, N. A.; Love, J. A.; Takacs, C. J.; Sadhanala, A.; Beavers, J.
652 K.; Collins, S. D.; Huang, Y.; Wang, M.; Friend, R. H.; Bazan, G. C.;
653 et al. Harvesting the Full Potential of Photons with Organic Solar
654 Cells. *Adv. Mater.* **2016**, *28*, 1482–1488.
- 655 (62) Veldman, D.; Meskers, S. C. J.; Janssen, R. A. J. The Energy of
656 Charge–Transfer States in Electron Donor-Acceptor Blends: Insight
657 into the Energy Losses in Organic Solar Cells. *Adv. Funct. Mater.* **2009**,
658 *19*, 1939–1948.
- 659 (63) Hu, X.; Yi, C.; Wang, M.; Hsu, C.-H.; Liu, S.; Zhang, K.; Zhong,
660 C.; Huang, F.; Gong, X.; Cao, Y. High-Performance Inverted Organic
661 Photovoltaics with over 1- μm Thick Active Layers. *Adv. Energy Mater.*
662 **2014**, *4*, 1400378.
- 663 (64) Sun, Y.; Seo, J. H.; Takacs, C. J.; Seifert, J.; Heeger, A. J.
664 Inverted Polymer Solar Cells Integrated with a Low-Temperature-
665 Annealed Sol-Gel-Derived ZnO Film as an Electron Transport Layer.
666 *Adv. Mater.* **2011**, *23*, 1679–1683.
- 667 (65) Lou, S. J.; Szarko, J. M.; Xu, T.; Yu, L.; Marks, T. J.; Chen, L. X.
668 Effects of Additives on the Morphology of Solution Phase Aggregates
669 Formed by Active Layer Components of High-Efficiency Organic
670 Solar Cells. *J. Am. Chem. Soc.* **2011**, *133*, 20661–20663.
- 671 (66) Sharenko, A.; Gehrig, D.; Laquai, F.; Nguyen, T.-Q. The Effect
672 of Solvent Additive on the Charge Generation and Photovoltaic
673 Performance of a Solution-Processed Small Molecule:Perylene
674 Diimide Bulk Heterojunction Solar Cell. *Chem. Mater.* **2014**, *26*,
675 4109–4118.
- 676 (67) Eastham, N. D.; Logsdon, J. L.; Manley, E. F.; Aldrich, T. J.;
677 Leonardi, M. J.; Wang, G.; Powers-Riggs, N. E.; Young, R. M.; Chen,
678 L. X.; Wasielewski, M. R.; et al. Hole-Transfer Dependence on Blend
679 Morphology and Energy Level Alignment in Polymer: ITIC
680 Photovoltaic Materials. *Adv. Mater.* **2018**, *29*, 1704263.
- 681 (68) Chen, S.; Liu, Y.; Lin, Z.; Chow, P. C. Y.; Zheng, W.; Zhang, G.;
682 Wei, M.; He, Y. A Wide-Bandgap Donor Polymer for Highly Efficient
683 Non-Fullerene Organic Solar Cells with a Small Voltage Loss. *J. Am.*
684 *Chem. Soc.* **2017**, *139*, 6298–6301.
- 685 (69) Baran, D.; Kirchartz, T.; Wheeler, S.; Dimitrov, S.; Abdelsamie,
686 M.; Gorman, J.; Ashraf, R.; Holliday, S.; Wadsworth, A.; Gasparini, N.;
687 et al. Reduced Voltage Losses Yield 10% and > 1V Fullerene Free
688 Organic Solar Cells. *Energy Environ. Sci.* **2016**, *9*, 3783–3793.
- 689 (70) Wei, Z.; Xi, H.; Dong, H.; Wang, L.; Xu, W.; Hu, W.; Zhu, D.
690 Blending Induced Stack-Ordering and Performance Improvement in a
691 Solution-Processed *n*-Type Organic Field-Effect Transistor. *J. Mater.*
692 *Chem.* **2010**, *20*, 1203–1207.
- 693 (71) Faist, M. A.; Shoaee, S.; Tuladhar, S.; Dibb, G. F. A.; Foster, S.;
694 Gong, W.; Kirchartz, T.; Bradley, D. D. C.; Durrant, J. R.; Nelson, J.
695 Understanding the Reduced Efficiencies of Organic Solar Cells
696 Employing Fullerene Multiadducts as Acceptors. *Adv. Energy Mater.*
697 **2013**, *3*, 744–752.
- 698 (72) Yang, B.; Cox, J.; Yuan, Y.; Guo, F. Increased Efficiency of Low
699 Band Gap Polymer Solar Cells at Elevated Temperature and Its
700 Origins. *Appl. Phys. Lett.* **2011**, *99*, 133302.
- 701 (73) Tan, M. J.; Zhong, S.; Li, J.; Chen, Z.; Chen, W. Air-Stable
702 Efficient Inverted Polymer Solar Cells Using Solution-Processed
703 Nanocrystalline ZnO Interfacial Layer. *ACS Appl. Mater. Interfaces*
704 **2013**, *5*, 4696–4701.